

# Atom-light hybrid interferometer for atomic sensing with quantum memory

Xingchang Wang,<sup>1</sup> Xinyun Liang,<sup>1</sup> Liang Dong,<sup>1</sup> Ying Zuo,<sup>2</sup> Jianmin Wang,<sup>3</sup> Dasen Yang,<sup>1,2</sup> Linyu Chen,<sup>1</sup> Georgios A. Siviloglou,<sup>4,5,1</sup> Z. Y. Ou,<sup>3,†</sup> and J. F. Chen,<sup>1,†</sup>

<sup>1</sup>*Department of Physics, Southern University of Science and Technology, Shenzhen 518055, China*

<sup>2</sup>*International Shenzhen Quantum Academy, Shenzhen 518048, China*

<sup>3</sup>*Department of Physics, City University of Hong Kong,*

*83 Tat Chee Avenue, Kowloon, Hong Kong, China*

<sup>4</sup>*Department of Physics, University of Crete, 71003, Heraklion, Greece*

<sup>5</sup>*Institute of Electronic Structure and Laser (IESL), FORTH, 71110, Heraklion, Greece*

(Dated: January 27, 2026)

Quantum memories feature a reversible conversion of optical fields into long-lived atomic spin waves, and are therefore ideal for operating as sensitive atomic sensors. However, up to now, atom-light interferometers have lacked an efficient approach to exploit their ultimate atomic sensing performance, since an extra optical delay line is required to compensate for the memory time. Here, we report a new protocol that records the photocurrent via heterodyne mixing with a stable local oscillator. The obtained complex quadrature amplitude that carries information imprinted on its phase by an external magnetic field, is successfully recovered from the interference patterns between the light and the atomic spin wave, without the stringent requirement of having them overlap in time. Our results reveal that the sensitivity scales favorably with the lifetime of the quantum memory. Our work may have important applications in building distributed quantum networks through quantum memory-assisted atom-light interferometers.

Atom-light interferometers utilize flying photons and atoms carrying atomic coherence as two distinct interferometric arms. In such systems, photons serve as carriers of quantum information capable of propagating over long distances, while localized atomic qubits act as efficient units for computation and sensing. The recent developments in atom-light hybrid interferometers have demonstrated that the transformation processes compatible with memory implement coherent conversion between photons and long-lived atomic coherence and reproduce first- and second-order interference between atoms and light [1–4]. Using the core principle common to both optical and atomic interferometry, namely interference between atoms and between light pulses, atomic sensors can be used to precisely probe diverse physical quantities from magnetic or electric fields and from gravitation to inertia [5–9]. The atomic arm of an atom-light hybrid interferometer is well qualified to implement sensing, provided that the phase difference between the atomic and the photonic states is measurable.

The stored atomic coherence is considered as an atomic spin wave converted from an optical wave, and the lifetime of this coherence ranges from sub-microseconds to seconds for atomic ensembles [10–15]. Following phase sensing within the memory lifetime, the atomic spin wave needs to be combined with the other optical arm at the second beam splitter to regenerate interference. Critically, this architecture faces a fundamental challenge: the read-out signal from the stored atomic spin state is temporally separated from the photons emitted earlier. Only if these photons propagate through a long-distance optical delay path can they interfere with the atomic state.

Although interference can in principle be restored using filtering and the aforementioned optical delay lines [16], photon transmission losses severely degrade the interference visibility as the storage time increases. Consequently, effective encoding of phase information in existing implementations is constrained to the optical arm, whereas the atomic arm has yet to demonstrate efficient sensing.

To avoid long optical delay lines, we propose to let the atom-light interferometer work as an unbalanced Mach-Zehnder interferometer (MZI), complemented by homodyne detection (HD) with a strong coherent local oscillator (LO) and the recording of the quadrature amplitude and phase of the optical field of the interferometer [17]. It has recently been demonstrated that the direct addition of the photocurrent appearing in HD could still lead to interference due to the addition of the amplitudes of the light fields, even though the path imbalance of the MZI is beyond coherence length of the input field [18, 19]. By recording the quadrature amplitude instead of the intensity of the optical field, phase information is preserved in the electronic signals converted from photodetectors. In the past, similar schemes of MZIs with HD have been used to measure the phase shifts appearing in the dispersive regime of neutral atoms [20–24].

In this Letter, we propose and demonstrate a new measurement protocol for atomic sensing based on an atom-light hybrid interferometer and amplitude measurement by HD. We utilize an elongated, laser-cooled atomic ensemble in a magneto-optical trap (MOT), in which a linear beam-splitter-type atom-light interaction is applied and photons are converted into atomic coherence

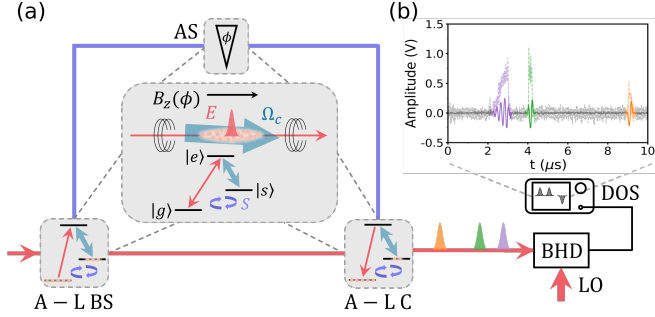


FIG. 1. Schematic setup. (a) An elongated, laser-cooled atomic ensemble serves as an atom-light beam splitter (A-L BS), atomic sensor (AS), and coupler (A-L C). A strong control light denoted as  $\Omega_c$  couples the signal field  $E$  and atomic coherence denoted as  $S$ , which accumulates a phase  $\phi$  in the presence of an external magnetic field  $B_z$  in the  $z$ -direction. The balanced homodyne detector (BHD) with a strong local oscillator (LO) records the quadrature amplitude and phase of the light signal. (b) The raw electronic output of BHD on a digital oscilloscope (DOS) is shown as a solid line. The dashed line is pulse profile recorded by photomultiplier. The purple, green, and orange lines represent the transmitted signal and multiple readouts of the memory.

with a phase controlled by an external magnetic field. The amplitude and phase of the transmitted and retrieved optical fields are recorded by beating with an LO in a balanced homodyne detector (BHD) as introduced in Ref. [18]. For the proof-of-principle, we show that the magnetic-field-controlled interference pattern is recovered by direct amplitude addition of the photocurrents without a second beam splitter and an optical delay line. The systematic errors and classical noise are well-controlled in our system, so that the precision of the magnetic field measurements is inversely proportional to the memory lifetime. In particular, an atom-light interferometer with a long memory lifetime can enable distributed quantum sensing [25–28]. Some plausible schemes have been put forward based on quantum communication using entangled particles [29, 30], and quantum repeaters [31].

Similar to unbalanced MZIs, we consider the time-separated signal fields transmitted (T) and retrieved (R) from the atomic ensemble; both of them appear as the optical mode outputs with amplitude  $E$  and frequency  $\omega_S$  of the atom-light interferometer:  $E_{TaT}(t)e^{-i\omega_S t}$  and  $E_{RaR}(t - \Delta\tau)e^{-i\omega_S(t - \Delta\tau)}$ . Here,  $a_j(t)$ , ( $j = T, R$ ) are the normalized pulse profiles, and  $\Delta\tau$  is the storage time for the atomic spin mode of the atom-light interferometer. In particular, the output of the HD is  $i_{HD}(t) \propto |\mathcal{E}|X(t)$ , where  $|\mathcal{E}|$  is the amplitude of the LO and  $X(t) = Ea(t)e^{-i\delta\omega t}e^{i\delta\phi} + c.c.$  is the quadrature-phase amplitude of the signal field;  $\delta\omega = \omega_{LO} - \omega_S$  and  $\delta\phi = \phi_{LO} - \phi_S$  are the frequency and phase differences between the signal field and the LO, respectively.

We measure from the HD the photocurrent signals of the balanced detector as  $i_T(t) \propto |\mathcal{E}|X_T(t)$  and  $i_R(t) \propto |\mathcal{E}|X_R(t)$ . By adding them together, we have  $i_+(t) = i_T(t) + i_R(t) \propto |\mathcal{E}|[X_T(t) + X_R(t)]$ . The power of the photocurrent is proportional to the average of  $i_+^2(t)$ , which is (see Appendix)

$$\langle i_+^2(t) \rangle \approx 2K|\mathcal{E}|^2(I_T + I_R)[1 + \mathcal{V}_0 \cos(\delta\omega\Delta\tau - \Delta\phi)], \quad (1)$$

where  $K$  corresponds to the response of the homodyne detector,  $\mathcal{V}_0 = 2\sqrt{I_T I_R}/(I_T + I_R)$  is the interference visibility,  $I_j = |E_j|^2$ , ( $j = T, R$ ) are the light intensities, and  $\Delta\phi = \delta\phi_T - \delta\phi_R$  is the accumulated phase during storage.

The stored collective excitation in an ensemble of  $N_a$  atoms can be written as  $|\psi(t)\rangle = \hat{S}^\dagger(t)|g_1, \dots, g_j, \dots, g_{N_a}\rangle$ , where  $\hat{S}(t) = (1/\sqrt{N_a})\sum_j \exp[-i\Delta\mathbf{k} \cdot \mathbf{r}_j(t) + i\Delta\omega_{gs}t] |g\rangle_j |s\rangle$  is the collective atomic excitation operator of the spin wave.  $\Delta\mathbf{k} = \mathbf{k}_c - \mathbf{k}_p$  is the wavevector of the spin wave depending on the control and signal beams.  $\mathbf{r}_j(t)$  is the position vector of the  $j$ -th excited atom at time  $t$ , related to the motion-type parameter sensing [5, 6, 32].  $\Delta\omega_{gs}$  is the frequency shift between the two atomic states  $|g\rangle$  and  $|s\rangle$  subjected to an external field. More specifically,  $\Delta\omega_{gs} = \mu_B(m_{gg} - m_{gs})B_z/\hbar$  is the Zeeman shift under the influence of a magnetic field  $B_z$  with the Bohr magneton  $\mu_B$ , the Landé  $g$ -factors, and the magnetic sublevels  $m_{g(s)}$ . If, for simplicity, we let  $\gamma$  be the gyromagnetic ratio instead of  $\mu_B(m_{gg} - m_{gs})/\hbar$ , then the phase shift of the stored spin wave can be written as  $\Delta\phi = \gamma B_z \Delta\tau$ . In our case,  $\gamma \approx 2\pi \cdot 18.8 \text{ GHz/T}$  for  $^{85}\text{Rb}$  with the specific Zeeman states  $|g : 5^2S_{1/2}, F = 2, m_F = 2\rangle$  and  $|s : 5^2S_{1/2}, F = 3, m_F = 2\rangle$  [33].

For a typical MZI scheme, in order to let the signals propagating through the long and short paths combine again at a second beam splitter to form an interference fringe, an extra fiber needs to be inserted to delay the earlier signal. Taking the case with a storage time  $\Delta\tau = 15 \mu\text{s}$  as an example, a 3 km fiber delay line is required. Note that at a fiber loss rate at 795 nm of  $\alpha = 3 \text{ dB/km}$ , an attenuation of 9 dB is introduced. Here, following the method in Ref. [18], we employ an HD to measure the quadrature-phase amplitudes of the two signal pulses by introducing an LO, which comes from a laser injection-locked to the signal laser, beating with the signal light, as shown in Fig. 1. The output of the 75 MHz bandwidth BHD is monitored by a fast digitizer with a 100 MHz sampling rate, corresponding to an effective bandwidth 50 MHz. By adding the recorded photocurrents from the two pulses after an electronic delay equal to the storage time, we obtain  $i_+(t)$  (see Appendix).

As in Fig. 2(a), the widths of the write and read pulses are  $t_w = 2 \mu\text{s}$  and  $t_r = 3 \mu\text{s}$ , respectively, while the widths of the T and R pulses are around  $1 \mu\text{s}$  due to the large Rabi frequency of the control light  $\Omega_c$ . The stor-

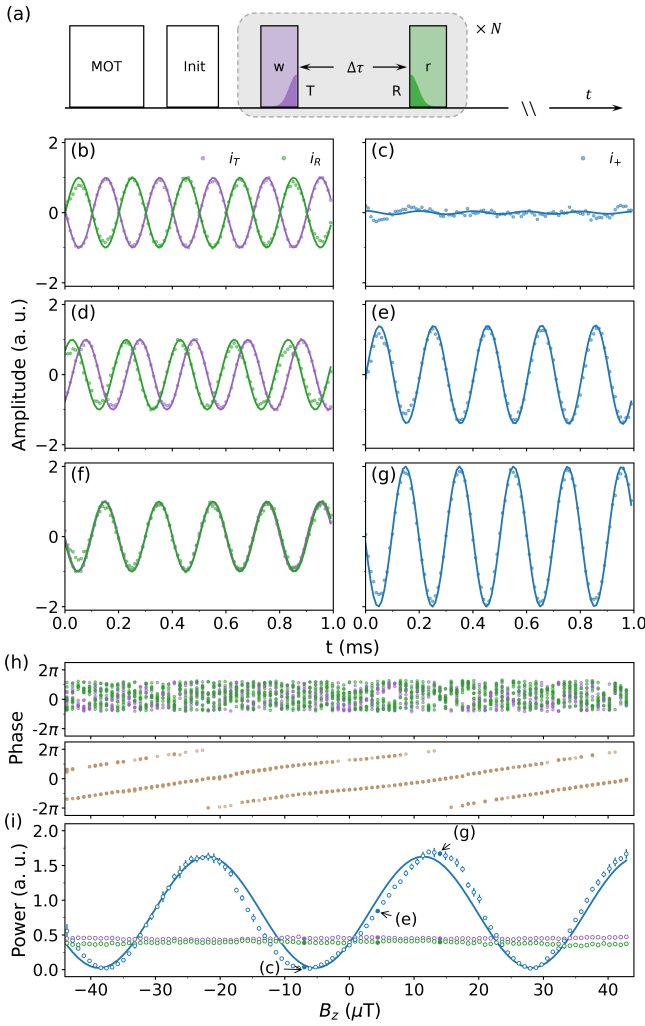


FIG. 2. (a) The measurement sequence for directly comparing transmitted and retrieved pulses, in which the storage time is  $\Delta\tau = 5\ \mu\text{s}$ . (b)-(g) Beating patterns between the signal and local oscillator in the balanced detector with a frequency difference  $\delta\omega/2\pi = 5\ \text{kHz}$ ; the purple and green dots are experimental data for the transmitted  $i_T$  and retrieved signal  $i_R$ , and the solid curve represents a fit to the data. The phase differences for (b):  $\pi$ , (d):  $\frac{\pi}{2}$ , and (f): 0. (c), (e), and (g) are the amplitudes of the addition in blue, corresponding to the filled points in (i). (h) The phase difference between LO and T is plotted as purple dots, and that between LO and R is plotted as green dots. The relative phase between T and R is plotted as yellow dots as a function of the scanned magnetic field. (i) Recovery of the interference fringes using the average power of the addition of the T and R beating patterns. The dots represent experimental data, and the solid line is the fitted curve.

age time  $\Delta\tau$  is  $5\ \mu\text{s}$  and the total duration of each measurement window  $t_{\text{tot}}$  is  $10\ \mu\text{s}$ . In each cycle after MOT preparation, we apply  $N = 100$  measurement repetitions. We scan the atomic phase of the interferometer using a magnetic field along the  $z$ -direction, generated by two

Helmholtz coils, with a scanning speed slower than the MOT repetition rate. To eliminate the influence of the sub-hertz frequency drift, we detune the LO with respect to the signal light by  $\delta\omega/2\pi = 5\ \text{kHz}$ , so that the HD becomes a heterodyne detection scheme. These recorded signals,  $i_T(t)$ ,  $i_R(t)$ , and  $i_+(t)$ , for various  $\Delta\phi$  induced by the magnetic field  $B_z$ , are shown in Figs. 2(b)-(g), in the form of pulse area integration, with (b), (d), and (f) showing a clear beat frequency  $\delta\omega$  in  $i_T(t)$ ,  $i_R(t)$ , and the summation  $i_+(t)$  of T and R in (c), (e), and (g), showing destructive to constructive interference. In Fig. 2(h), we record the phase difference variation as a function of the applied magnetic field. Due to the random phase introduced by air flow, the phases of T (purple dots) and R (green dots) themselves show no obvious relation to the magnetic field. While the phase difference (yellow dots) between them shows a clearly linear accumulation due to the increase of the magnetic field, but it also has an ambiguity of  $n \cdot 2\pi$ . The output power of the HD, recorded by a spectrum analyzer, is proportional to  $\langle i_+^2 \rangle$ . As a result, we plot the power of the current addition  $i_+$  while varying the magnetic field  $B_z$ , as shown as dots in Fig. 2(i). The recovered interference pattern is satisfactorily consistent with the fitted curve from Eq. (1). The difference between theory and experiment is attributed to the imperfect beating patterns.

If we consider the response function of the homodyne detector to be  $k(t)$ , the visibility is written as (see [Appendix](#))

$$\mathcal{V}(\delta\omega) \approx \mathcal{V}_0 \int d\omega \tilde{\mathcal{K}}(\omega) \tilde{\mathcal{A}}_{TR}(\delta\omega - \omega), \quad (2)$$

where  $\tilde{\mathcal{K}}(\omega)$  and  $\tilde{\mathcal{A}}_{TR}(\omega)$  are the Fourier transforms of  $\mathcal{K}(\tau) = \int dt k(t)k(t + \tau)$  and  $\mathcal{A}_{TR}(\tau)$ , respectively.  $\mathcal{A}_{TR}(\tau) = \langle a_T(t)a_R(t - \tau) \rangle$  is the pulse amplitude cross-correlation function of T and R.  $\tilde{\mathcal{K}}(\omega)$  is the response spectrum of the detector, and  $\tilde{\mathcal{A}}_{TR}(\omega)$  is the pulse spectrum cross-correlation. Here, we discuss two specific cases depending on the response function  $k(t)$  and the pulse profile  $a(t)$ : (I) If the response function  $k(t)$  is very slow, such that  $\delta\nu_k \ll \delta\nu_a$ , where  $\delta\nu_k$  and  $\delta\nu_a$  are the bandwidths of  $\tilde{\mathcal{K}}(\omega)$  and  $\tilde{\mathcal{A}}_{TR}(\omega)$ , we can consider the response spectrum  $\tilde{\mathcal{K}}(\omega)$  to be a delta-function; thus  $\mathcal{V}(\delta\omega) \approx \mathcal{V}_0 \tilde{\mathcal{A}}_{TR}(\delta\omega)$ . (II) If the response function  $k(t)$  is very fast, such that  $\delta\nu_k \gg \delta\nu_a$ , we can consider the pulse spectrum  $\tilde{\mathcal{A}}_{TR}(\omega)$  to be a delta-function, i.e.,  $\tilde{\mathcal{A}}_{TR}(\omega) \approx \mathcal{A}_{TR}(0)\delta(\omega)$ ; then Eq. (2) gives  $\mathcal{V}(\delta\omega) \approx \mathcal{V}_0 \mathcal{A}_{TR}(0) \tilde{\mathcal{K}}(\delta\omega)$ .

Since the data analysis method in Fig. 2 is by pulse area integration (see [Appendix](#)), the result corresponds to the slow detector case (I), where the acceptable  $\delta\omega$  between the LO and the signal field is limited by the pulse spectral width. Next, we will see that the tolerable limit extends to a large  $\delta\omega$  in this protocol by using a fast detector as in case (II), which allows point-to-point addition

of the photocurrent data,  $i_T$  and  $i_R$ , leading to the result that the visibility is only limited by the response function  $k(t)$  of the broadband BHD (50 MHz in our experimental setup), according to Eq. (2). In this case, the visibility is proportional to the pulse correlation function  $\mathcal{A}_{TR}(0)$ , which can be maximized by matching the pulse shapes of T and R. However, the T and R pulses are asymmetric, which is typical for the optical storage process [34]. In order to obtain acceptable interference visibility, we alternatively apply a multipulse memory operation sequence with multiple readout pulses [35], as shown in Fig. 3(a). This new scheme facilitates a perfect match between the temporal profiles of the retrieved pulses; we select the first (r1) and second (r2) readout signal pulses as the data for  $i_T$  and  $i_R$ . In this case, the width of the write pulse is kept at  $t_w = 2 \mu\text{s}$ , and the widths of the two readout pulses are both  $t_r = 200 \text{ ns}$ . In order to maintain a satisfactory readout efficiency, the first readout pulse is applied immediately after the write pulse. The storage time between the two readout pulses  $\Delta\tau$  is  $5 \mu\text{s}$ , and the total duration of each measurement is still  $10 \mu\text{s}$ . The ratio between the two readout pulses is adjusted by varying the intensity and the pulse width of the control field.

With this time-sequence scheme, it is now fair to compare the visibility given by Eq. (2) in the two cases with a fast and a slow detector, respectively. Fig. 3(b) shows case (I), and the visibility of recovered interference is severely reduced when the frequency difference  $\delta\omega/2\pi$  changes from 5 kHz (blue circles) to 4 MHz (blue triangles). However, for case (II), when  $\delta\omega/2\pi = 4 \text{ MHz}$ , visibility does not change (see [Appendix](#)) as shown in Fig. 3(c). To show the full trend between visibility and frequency difference more clearly, we depict them in Fig. 3(d) as blue and red points for case (I) and case (II), respectively. The solid curves are a Gaussian function fit to the decays of the two cases by assuming that both the response function  $k(t)$  and the pulse profile  $a(t)$  have a Gaussian shape. Specifically, the bandwidths of the Gaussian fits are  $\delta\nu_{\mathcal{V}}^{(I)} \approx 3.84 \pm 1.94 \text{ MHz}$  and  $\delta\nu_{\mathcal{V}}^{(II)} \approx 46.01 \pm 20.00 \text{ MHz}$ , respectively. This fitting result is evidently limited by the pulse spectrum profile  $\delta\nu_a \approx 2.21 \text{ MHz}$  and the detector response  $\delta\nu_k \approx 50 \text{ MHz}$ , as predicted by Eq. (2). The labeled solid filled data points correspond to the respective cases in Figs. 3(b) and (c).

As shown in Fig. 2 and Fig. 3, the interferometric phase is accumulated through the stored atomic spin wave under the influence of a magnetic field along the z-axis,  $B_z$ . During operation around the maximum slope  $\partial\langle i_+^2(t) \rangle / \partial B_z$ , the power variation  $\delta\langle i_+^2(t) \rangle$  determines the magnetic field uncertainty  $\delta B_z = \delta\langle i_+^2(t) \rangle / [\partial\langle i_+^2(t) \rangle / \partial B_z] \propto 1/(\gamma\Delta\tau)$ . The memory-based protocol yields a coherence-time scaling that is inversely proportional to storage time  $\Delta\tau$ . To observe the dependence of measurement uncertainty on storage time, we

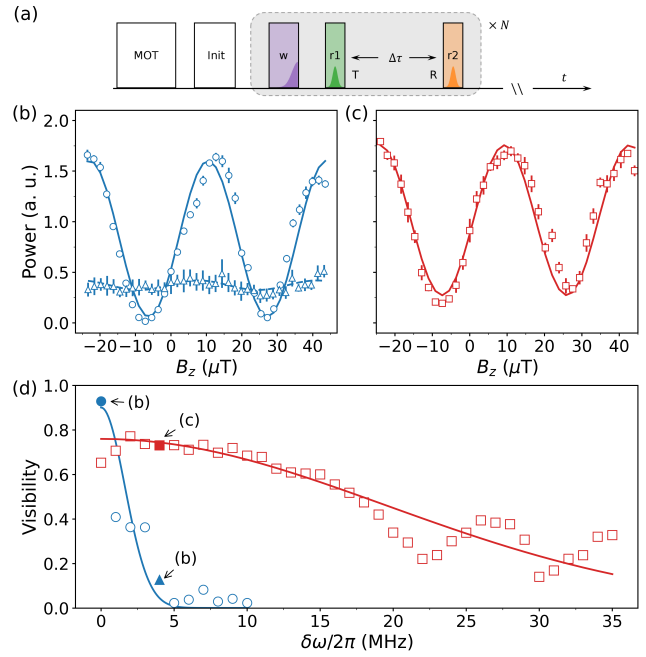


FIG. 3. (a) The measurement sequence with multiple readout pulses. The first and second retrieved signals  $r_1$  and  $r_2$  are denoted as T and R in Fig. 2(a), and their storage time is  $\Delta\tau = 5 \mu\text{s}$ . (b) The recovered interference fringe pattern obtained using a slow detector, where frequency differences  $\delta\omega/2\pi = 5 \text{ kHz}$  and  $\delta\omega/2\pi = 4 \text{ MHz}$  are marked as circles and triangles, respectively; the solid lines are the fitting curves. (c) The recovered interference fringe for the fast detector case, with a frequency difference  $\delta\omega/2\pi = 4 \text{ MHz}$ ; the square points and solid line are the experimental data and the fitting curve, respectively. (d) Visibility as a function of the frequency shift of the LO, i.e.,  $\delta\omega$ . The visibility of the curves in (b) and (c) is marked by the corresponding filled data points.

vary the storage time  $\Delta\tau$  from  $5 \mu\text{s}$  to  $15 \mu\text{s}$  between the first and second readout pulses within the coherence lifetime  $\tau \approx 35 \mu\text{s}$ . The measurement data are plotted in Fig. 4, during which  $\delta\omega/2\pi = 5 \text{ kHz}$ , where each point corresponds to a total integration time  $t_{int} = 1 \text{ s}$ . The measurement precision  $\delta B$  follows the  $1/\Delta\tau$  scaling up to  $\Delta\tau = 15 \mu\text{s}$ , beyond which it slightly deviates due to fluctuations of the uncompensated magnetic fields in an unshielded MOT system. The coherence lifetime is currently determined by the wavelength of the stored spin wave as well as the expansion and free fall of the atomic ensemble. These commonly encountered limitations can be alleviated by utilizing a collinear configuration of the control and signal beams [10, 14], for which a best coherence time  $\tau = 1.24 \text{ ms}$  has been reported [14]. The precision at the optimal measurement time  $\tau/2$  [36] is shown as the square point in Fig. 4. By confining atoms in an optical dipole trap (ODT) [11–13], the precision can reach the red region in Fig. 4; such a system can even hold a minute-scale coherence lifetime, giving a precision of pT-level (red triangle) [12].

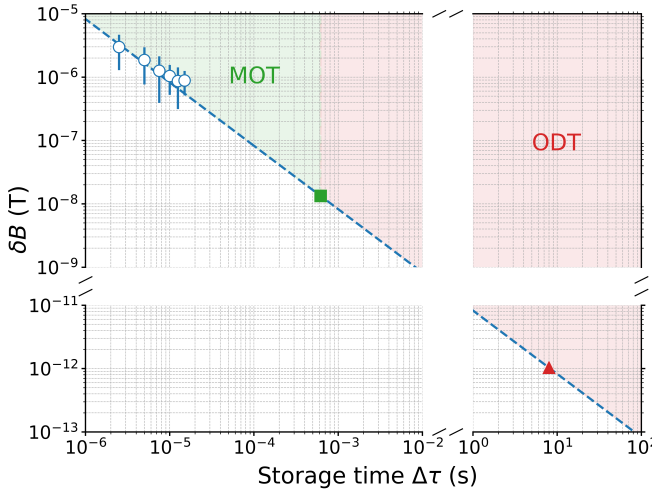


FIG. 4. The magnetic field measurement precision of the interferometer versus storage time  $\Delta\tau$ . The circle points are the measurement data and the dashed line is the fitting curve with a  $\Delta\tau^{-1}$  scaling. Error bars indicate the standard deviation of all measurements. The green and red regions represent atoms trapped in the MOT and the ODT, respectively. The square and triangle points are the optimal measurement times for atoms held in the MOT, and the ODT, from Ref. [14] and Ref. [12], respectively.

In summary, we demonstrate a new protocol for operating an atom-light hybrid interferometer for magnetic field sensing enabled by quantum storage. We experimentally show that, via HD, the interference between the transmitted and subsequently retrieved signals is recovered from data analysis of photocurrents without any time overlap between the two signals. We therefore verify that the quantum memory is an instrumental feature of our magnetometry, acting as a coherent process that leads to the accumulation of phase. Moreover, extending the storage lifetime will directly improve the sensitivity. Compared to standard atom interferometers, the atom-light interferometer demonstrated here is predominantly limited by the photon number of the optical mode; this should be significantly smaller than the atom population, stemming from the beam-splitter-type interaction model. For an optical power of 10 to 100 nW, this corresponds to a photon flux of  $10^6$  photons per pulse. This satisfies the condition of being significantly smaller than the estimated atom population of  $10^9$  in our setup. Further optimizations can be implemented at this stage. The system remains highly sensitive to ambient magnetic fields, and magnetic shielding could be essential for reaching the level of state-of-the-art magnetometers.

Furthermore, the atom-light interferometer features both quantum memory and a beam-splitter-type interaction between atoms and light. It has already been demonstrated that second-order interference between atomic and photonic modes is achievable [3, 4]. A nonlocal interferometer composed of distributed atom-light interferom-

eters is promising for sensing physical quantities that can be converted into a phase accumulated by atoms alone (e.g., magnetic fields or gravity). With the convenience of a photonic arm, the flying photons emitted from each interferometer could implement a Bell-state measurement at a distant location. The architecture of a Very-Long-Baseline Interferometer [31, 37] is an attractive direction for building a quantum network of atomic sensors; alternatively, it could be used to measure worldwide dark matter or gravitational variations. In the other extreme of the small scale, arrays of atomic clouds are an interesting platform for measuring micro-scale gradient distributions of magnetic fields and gravitational forces [38]. If we assume  $M$  ensembles entangled via the DLCZ protocol realized with quantum memories, the sensitivity of such a quantum network of probes is expected to be improved by a factor of  $\sqrt{M}$  over the individual probes.

This work is supported by the National Natural Science Foundation of China (NSFC) through Grants No. 92476102, No. 12404409, No. 92265109, and No. 12474262, and by the General Research Fund from Hong Kong Research Grants Council through No. 11315822 and No. 11307625. J. F. C. acknowledges the Guangdong Key Project under Grant No. 2022B1515020096. G. A. S. acknowledges support from the Hellenic Foundation for Research and Innovation (H.F.R.I.) under Project No. 11496 (“PSEUDOTOP-POS”). X. W. acknowledges support from the SUSTech Presidential Postdoctoral Fellowship. J. W. acknowledges the support from City University of Hong Kong under Project No. 9610522.

- 
- [1] B. Chen, C. Qiu, S. Chen, J. Guo, L. Q. Chen, Z. Y. Ou, and W. Zhang, Atom-Light Hybrid Interferometer, *Phys. Rev. Lett.* **115**, 043602 (2015).
  - [2] R. Wen, C.-L. Zou, X. Zhu, P. Chen, Z. Y. Ou, J. F. Chen, and W. Zhang, Non-Hermitian Magnon-Photon Interference in an Atomic Ensemble, *Phys. Rev. Lett.* **122**, 253602 (2019).
  - [3] X. Wang, J. Wang, Z. Ren, R. Wen, C.-L. Zou, G. A. Siviloglou, and J. F. Chen, Quantum Interference between Photons and Single Quanta of Stored Atomic Coherence, *Phys. Rev. Lett.* **128**, 083605 (2022).
  - [4] K. Su, Y. Zhong, S. Zhang, J. Li, C.-L. Zou, Y. Wang, H. Yan, and S.-L. Zhu, Quantum interference between nonidentical single particles, *Phys. Rev. Lett.* **129**, 093604 (2022).
  - [5] Y.-A. Chen, X.-H. Bao, Z.-S. Yuan, S. Chen, B. Zhao, and J.-W. Pan, Heralded Generation of an Atomic NOON State, *Phys. Rev. Lett.* **104**, 043601 (2010).
  - [6] P.-C. Kuan, C. Huang, W. S. Chan, S. Kosen, and S.-Y. Lan, Large Fizeau’s light-dragging effect in a moving electromagnetically induced transparent medium, *Nat. Commun.* **7**, 13030 (2016).
  - [7] P. Gomez, F. Martin, C. Mazzinghi, D. Benedicto Orenes, S. Palacios, and M. W. Mitchell, Bose-

- Einstein Condensate Comagnetometer, *Phys. Rev. Lett.* **124**, 170401 (2020).
- [8] Y. A. Yang, W.-T. Luo, J.-L. Zhang, S.-Z. Wang, C.-L. Zou, T. Xia, and Z.-T. Lu, Minute-scale Schrödinger-cat state of spin-5/2 atoms, *Nat. Photonics* **19**, 89 (2025).
- [9] Z. Ma, C. Han, Z. Tan, H. He, S. Shi, X. Kang, J. Wu, J. Huang, B. Lu, and C. Lee, Adaptive cold-atom magnetometry mitigating the trade-off between sensitivity and dynamic range, *Sci. Adv.* **11**, eadtr3938 (2025).
- [10] B. Zhao, Y.-A. Chen, X.-H. Bao, T. Strassel, C.-S. Chuu, X.-M. Jin, J. Schmiedmayer, Z.-S. Yuan, S. Chen, and J.-W. Pan, A millisecond quantum memory for scalable quantum networks, *Nat. Phys.* **5**, 95 (2009).
- [11] R. Zhao, Y. O. Dudin, S. D. Jenkins, C. J. Campbell, D. N. Matsukevich, T. A. B. Kennedy, and A. Kuzmich, Long-lived quantum memory, *Nat. Phys.* **5**, 100 (2009).
- [12] Y. O. Dudin, L. Li, and A. Kuzmich, Light storage on the time scale of a minute, *Phys. Rev. A* **87**, 031801 (2013).
- [13] S.-J. Yang, X.-J. Wang, X.-H. Bao, and J.-W. Pan, An efficient quantum light–matter interface with sub-second lifetime, *Nat. Photonics* **10**, 381 (2016).
- [14] Y.-W. Cho, G. T. Campbell, J. L. Everett, J. Bernu, D. B. Higginbottom, M. T. Cao, J. Geng, N. P. Robins, P. K. Lam, and B. C. Buchler, Highly efficient optical quantum memory with long coherence time in cold atoms, *Optica* **3**, 100 (2016).
- [15] Y.-F. Hsiao, P.-J. Tsai, H.-S. Chen, S.-X. Lin, C.-C. Hung, C.-H. Lee, Y.-H. Chen, Y.-F. Chen, I. A. Yu, and Y.-C. Chen, Highly Efficient Coherent Optical Memory Based on Electromagnetically Induced Transparency, *Phys. Rev. Lett.* **120**, 183602 (2018).
- [16] R. Erdmann, D. Branning, W. Grice, and I. A. Walmsley, Restoring dispersion cancellation for entangled photons produced by ultrashort pulses, *Phys. Rev. A* **62**, 053810 (2000).
- [17] H. Yuen and J. Shapiro, Optical communication with two-photon coherent states—Part I: Quantum-state propagation and quantum-noise, *IEEE Trans. Inf. Theory* **24**, 657 (1978).
- [18] Y. Zhang, X. Tang, X. Guo, L. Cui, X. Li, and Z. Y. Ou, Optical interference by amplitude measurement, *Phys. Rev. Research* **7**, 013255 (2025).
- [19] X. Tang, Y. Zhang, X. Guo, L. Cui, X. Li, and Z. Y. Ou, Phase-dependent Hanbury-Brown and Twiss effect for the complete measurement of the complex coherence function, *Light Sci. Appl.* **14**, 46 (2025).
- [20] M. Xiao, Y.-Q. Li, S.-Z. Jin, and J. Gea-Banacloche, Measurement of Dispersive Properties of Electromagnetically Induced Transparency in Rubidium Atoms, *Phys. Rev. Lett.* **74**, 666 (1995).
- [21] Q. A. Turchette, C. J. Hood, W. Lange, H. Mabuchi, and H. J. Kimble, Measurement of Conditional Phase Shifts for Quantum Logic, *Phys. Rev. Lett.* **75**, 4710 (1995).
- [22] O. Schmidt, R. Wynands, Z. Hussein, and D. Meschede, Steep dispersion and group velocity below  $c/3000$  in coherent population trapping, *Phys. Rev. A* **53**, R27 (1996).
- [23] A. S. Zibrov, M. D. Lukin, L. Hollberg, D. E. Nikonov, M. O. Scully, H. G. Robinson, and V. L. Velichansky, Experimental Demonstration of Enhanced Index of Refraction via Quantum Coherence in Rb, *Phys. Rev. Lett.* **76**, 3935 (1996).
- [24] S. A. Aljunid, M. K. Tey, B. Chng, T. Liew, G. Maslenikov, V. Scarani, and C. Kurtsiefer, Phase Shift of a Weak Coherent Beam Induced by a Single Atom, *Phys. Rev. Lett.* **103**, 153601 (2009).
- [25] V. Giovannetti, S. Lloyd, and L. Maccone, Quantum-enhanced measurements: Beating the standard quantum limit, *Science* **306**, 1330 (2004).
- [26] X. Guo, C. R. Breum, J. Borregaard, S. Izumi, M. V. Larsen, T. Gehring, M. Christandl, J. S. Neergaard-Nielsen, and A. U. L., Distributed quantum sensing in a continuous-variable entangled network, *Nat. Phys.* **16**, 281 (2020).
- [27] L.-Z. Liu, Y.-Z. Zhang, Z.-D. Li, R. Zhang, X.-F. Yin, Y.-Y. Fei, L. Li, N.-L. Liu, F. Xu, Y.-A. Chen, and J.-W. Pan, Distributed quantum phase estimation with entangled photons, *Nat. Photonics* **15**, 137 (2021).
- [28] B. K. Malia, M.-R. J. Wu, Yunfan, and M. A. Kasevich, Distributed quantum sensing with mode-entangled spin-squeezed atomic states, *Nature* **612**, 661 (2022).
- [29] Z. Zhang and Q. Zhuang, Distributed quantum sensing, *Quantum Sci. Technol.* **6**, 043001 (2021).
- [30] Y. Yang, B. Yadin, and Z.-P. Xu, Quantum-Enhanced Metrology with Network States, *Phys. Rev. Lett.* **132**, 210801 (2024).
- [31] D. Gottesman, T. Jennewein, and S. Croke, Longer-Baseline Telescopes Using Quantum Repeaters, *Phys. Rev. Lett.* **109**, 070503 (2012).
- [32] X. Wang, J. Wang, Y. Zuo, L. Dong, G. A. Siviloglou, and J. Chen, Thermometry utilizing stored short-wavelength spin waves in cold atomic ensembles, *Chin. Phys. B* **32**, 074206 (2023).
- [33] D. A. Steck, Rubidium 85 D Line Data, available online at <http://steck.us/alkalidata> (revision 2.3.4, 8 August 2025).
- [34] I. Novikova, A. V. Gorshkov, D. F. Phillips, A. S. Sørensen, M. D. Lukin, and R. L. Walsworth, Optimal Control of Light Pulse Storage and Retrieval, *Phys. Rev. Lett.* **98** (2007).
- [35] K. F. Reim, J. Nunn, X.-M. Jin, P. S. Michelberger, T. F. M. Champion, D. G. England, K. C. Lee, W. S. Kolthammer, N. K. Langford, and I. A. Walmsley, Multipulse Addressing of a Raman Quantum Memory: Configurable Beam Splitting and Efficient Readout, *Phys. Rev. Lett.* **108**, 263602 (2012).
- [36] J. F. Barry, J. M. Schloss, E. Bauch, M. J. Turner, C. A. Hart, L. M. Pham, and R. L. Walsworth, Sensitivity optimization for NV-diamond magnetometry, *Rev. Mod. Phys.* **92**, 015004 (2020).
- [37] J. D. Monnier, Optical interferometry in astronomy, *Reports on Progress in Physics* **66**, 789 (2003).
- [38] D. Schäffner, T. Schreiber, F. Lenz, M. Schlosser, and G. Birk, Quantum sensing in tweezer arrays: Optical magnetometry on an individual-atom sensor grid, *PRX Quantum* **5**, 010311 (2024).

## Appendix

*Experimental setup details.* In the experiment illustrated in Fig. 1(a), an elongated laser-cooled  $^{85}\text{Rb}$  atomic ensemble loaded in a two-dimensional MOT acts as a beam splitter based on electromagnetically-induced transparency optical storage. Initially, the atoms are trapped and cooled for 18.7 ms. After MOT loading, we initialize all atoms into the ground state  $|g : 5^2S_{1/2}, F = 2, m_F = 2\rangle$  using 0.3 ms of optical pumping. The  $\sigma^+$  signal light  $E$ , resonant with the transition  $|g\rangle \rightarrow |e : 5^2P_{1/2}, F = 3, m_F = 3\rangle$ , passes through the atomic medium, which becomes transparent in the presence of a strong  $\sigma^+$  control light  $\Omega_c$ . This control beam is resonant with the optical transition  $|e\rangle \rightarrow |s : 5^2S_{1/2}, F = 3, m_F = 2\rangle$ . When the control light is switched off, the signal light is partially transmitted and is considered the transmission of the beam splitter, while the absorbed light is converted to a long-lived atomic collective excitation that leads to reflection. After a storage time of  $\Delta\tau$ , this stored excitation accumulates a phase  $\Delta\phi$  induced by the magnetic field  $B_z$  along the  $z$ -direction, which coincides with the long axis of the atomic cloud. A second control pulse reads out the stored atomic excitation, converting it back into the optical mode that constitutes the retrieved signal. This memory process is repeated  $N$  times before the next round of MOT loading. Each full cycle, including MOT loading and the write-read process, lasts 20 ms, within which the measurement window accounts for 1 ms.

*Visibility of direct current addition.* Taking the response function for the homodyne detector as  $k(t)$ , the output current is:

$$i_+(t) = i_T(t) + i_R(t) \propto |\mathcal{E}| \int d\tau k(t-\tau) [X_T(\tau) + X_R(\tau)], \quad (3)$$

where  $X_T(\tau) = E_T a_T(\tau) e^{-i\delta\omega\tau} e^{i\delta\phi_T} + \text{c.c.}$  and  $X_R(\tau) = E_R a_R(\tau - \Delta\tau) e^{-i\delta\omega(\tau-\Delta\tau)} e^{i\delta\phi_R} + \text{c.c.}$ , with  $a_j(\tau)$ , ( $j = T, R$ ), being the normalized pulse profiles satisfying  $\int d\tau a_j^2(\tau) = 1$ . All four correlation functions for the  $X_T$  and  $X_R$  are:

$$\begin{aligned} & \langle X_T(\tau) X_T(\tau') \rangle \\ &= \langle E_T a_T(\tau) E_T^* a_T(\tau') \rangle e^{-i\delta\omega(\tau-\tau')} + \text{c.c.} \\ &= I_T \mathcal{A}_{TT}(\tau - \tau') e^{-i\delta\omega(\tau-\tau')} + \text{c.c.}, \quad (4a) \\ & \langle X_R(\tau) X_R(\tau') \rangle \\ &= \langle E_R a_R(\tau - \Delta\tau) E_R^* a_R(\tau' - \Delta\tau) \rangle e^{-i\delta\omega(\tau-\tau')} + \text{c.c.} \end{aligned}$$

$$= I_R \mathcal{A}_{RR}(\tau - \tau') e^{-i\delta\omega(\tau-\tau')} + \text{c.c.}, \quad (4b)$$

$$\begin{aligned} & \langle X_T(\tau) X_R(\tau') \rangle \\ &= \langle E_T a_T(\tau) E_R^* a_R(\tau' - \Delta\tau) \rangle e^{-i\delta\omega(\tau-(\tau'-\Delta\tau))} e^{i\Delta\phi} + \text{c.c.} \\ &= \sqrt{I_T I_R} \mathcal{A}_{TR}(\tau - \tau' + \Delta\tau) e^{-i\delta\omega(\tau-\tau'+\Delta\tau)} e^{i\Delta\phi} + \text{c.c.}, \quad (4c) \end{aligned}$$

$$\begin{aligned} & \langle X_R(\tau) X_T(\tau') \rangle \\ &= \langle E_R a_R(\tau - \Delta\tau) E_T^* a_T(\tau') \rangle e^{-i\delta\omega((\tau-\Delta\tau)-\tau')} e^{-i\Delta\phi} + \text{c.c.} \\ &= \sqrt{I_R I_T} \mathcal{A}_{RT}(\tau - \tau' - \Delta\tau) e^{-i\delta\omega(\tau-\tau'-\Delta\tau)} e^{-i\Delta\phi} + \text{c.c.}, \quad (4d) \end{aligned}$$

where  $I_j = E_j E_j^*$  is the light intensity for  $j = T, R$ , and  $\mathcal{A}_{ij}(\tau) = \langle a_i(t) a_j(t-\tau) \rangle$  is the corresponding amplitude correlation function. The output power is proportional to:

$$\begin{aligned} \langle i_+^2(t) \rangle &= |\mathcal{E}|^2 \int d\tau d\tau' k(t-\tau) k(t-\tau') e^{-i\delta\omega(\tau-\tau')} \\ &\quad \cdot [I_T \mathcal{A}_{TT}(\tau - \tau') + I_R \mathcal{A}_{RR}(\tau - \tau')] \\ &\quad + \sqrt{I_T I_R} \mathcal{A}_{TR}(\tau - \tau' + \Delta\tau) e^{-i\delta\omega\Delta\tau} e^{i\Delta\phi} \\ &\quad + \sqrt{I_R I_T} \mathcal{A}_{RT}(\tau - \tau' - \Delta\tau) e^{i\delta\omega\Delta\tau} e^{-i\Delta\phi} + \text{c.c.} \quad (5) \end{aligned}$$

If the storage time  $\Delta\tau$  is significantly larger than the signal pulse width  $\Delta T_c$ , the amplitude correlation functions become  $\mathcal{A}_{TR}(\Delta\tau) = \mathcal{A}_{RT}(\Delta\tau) = 0$ . We use an electronic delay  $\Delta T_e$  to balance the storage delay; while the phase variation during storage is not compensated, resulting in:

$$\begin{aligned} \langle i_+^2(t) \rangle &= |\mathcal{E}|^2 \int d\tau d\tau' k(t-\tau) k(t-\tau') e^{-i\delta\omega(\tau-\tau')} \\ &\quad \cdot [I_T \mathcal{A}_{TT}(\tau - \tau') + I_R \mathcal{A}_{RR}(\tau - \tau')] \\ &\quad + \sqrt{I_T I_R} \mathcal{A}_{TR}(\tau - \tau') e^{-i\delta\omega\Delta\tau} e^{i\Delta\phi} \\ &\quad + \sqrt{I_R I_T} \mathcal{A}_{RT}(\tau - \tau') e^{i\delta\omega\Delta\tau} e^{-i\Delta\phi} + \text{c.c..} \\ &= |\mathcal{E}|^2 \int d\tau'' \mathcal{K}(\tau'') e^{-i\delta\omega\tau''} \\ &\quad \cdot [I_T \mathcal{A}_{TT}(\tau'') + I_R \mathcal{A}_{RR}(\tau'')] \\ &\quad + \sqrt{I_T I_R} \mathcal{A}_{TR}(\tau'') e^{-i\delta\omega\Delta\tau} e^{i\Delta\phi} \\ &\quad + \sqrt{I_R I_T} \mathcal{A}_{RT}(\tau'') e^{i\delta\omega\Delta\tau} e^{-i\Delta\phi} + \text{c.c..} \quad (6) \end{aligned}$$

where  $\mathcal{K}(\tau'') = \int d\tau k(t-\tau) k(t-\tau+\tau'')$ .

The speed of the detector with respect to the integration time can lead to simple analytical expressions for the visibility,  $\mathcal{V}$ :

(I) If the detector is very slow  $k(t-\tau)$  and  $k(t-\tau')$  can be taken equal to a constant number  $k$  over the integration with respect to  $\tau$  and  $\tau'$ :

$$\begin{aligned}
\langle i_+^2(t) \rangle &= k^2 |\mathcal{E}|^2 \left\{ I_T \left[ \int_{t_1}^{t_2} d\tau a_T(t-\tau) \right]^2 + I_R \left[ \int_{t_1}^{t_2} d\tau a_R(t-\tau) \right]^2 \right. \\
&\quad + \sqrt{I_T I_R} e^{-i\delta\omega\Delta\tau} e^{i\Delta\phi} \int_{t_1}^{t_2} d\tau a_T(t-\tau) \int_{t_1}^{t_2} d\tau a_R(t-\tau) \\
&\quad \left. + \sqrt{I_R I_T} e^{i\delta\omega\Delta\tau} e^{-i\Delta\phi} \int_{t_1}^{t_2} d\tau a_R(t-\tau) \int_{t_1}^{t_2} d\tau a_T(t-\tau) \right\} + c.c. \} \\
&\leq k^2 |\mathcal{E}|^2 (t_2 - t_1) \left[ I_T \langle \int_{t_1}^{t_2} d\tau a_T^2(t-\tau) \rangle + I_R \langle \int_{t_1}^{t_2} d\tau a_R^2(t-\tau) \rangle \right. \\
&\quad + \sqrt{I_T I_R} e^{-i\delta\omega\Delta\tau} e^{i\Delta\phi} \langle \sqrt{\int_{t_1}^{t_2} d\tau a_T^2(t-\tau) \int_{t_1}^{t_2} d\tau a_R^2(t-\tau)} \rangle \\
&\quad \left. + \sqrt{I_R I_T} e^{i\delta\omega\Delta\tau} e^{-i\Delta\phi} \langle \sqrt{\int_{t_1}^{t_2} d\tau a_R^2(t-\tau) \int_{t_1}^{t_2} d\tau a_T^2(t-\tau)} \rangle + c.c. \right]. \tag{7}
\end{aligned}$$

Here, we use the assumption that the integration region for  $d\tau$  and  $d\tau'$  is from the start time  $t_1$  to the end time  $t_2$ , then  $\int_{t_1}^{t_2} \int_{t_1}^{t_2} a(\tau)a(\tau')d\tau d\tau' \rightarrow [\int_{t_1}^{t_2} a(\tau)d\tau]^2$ , and Cauchy-Schwarz inequality  $[\int_{t_1}^{t_2} a(\tau)d\tau]^2 \leq (t_2 - t_1) \int_{t_1}^{t_2} d\tau [a(\tau)]^2$ . Finally, we get Eq. (1) of the main text

$$\langle i_+^2(t) \rangle \approx 2K|\mathcal{E}|^2(I_T + I_R)[1 + \mathcal{V}_0 \cos(\delta\omega\Delta\tau - \Delta\phi)], \tag{8}$$

where  $K = k^2$ , and  $\mathcal{V}_0 = 2\sqrt{I_T I_R}/(I_T + I_R)$ .

(II) If the detector is very fast,  $k(t-\tau)$ ,  $k(t-\tau')$  can take the form of a  $\delta$ -function:

$$\begin{aligned}
\langle i_+^2(t) \rangle &\approx |\mathcal{E}|^2 [I_T \mathcal{A}_{TT}(0) + I_R \mathcal{A}_{RR}(0) \\
&\quad + \sqrt{I_T I_R} \mathcal{A}_{TR}(0) e^{-i\delta\omega\Delta\tau} e^{i\Delta\phi} \\
&\quad + \sqrt{I_R I_T} \mathcal{A}_{RT}(0) e^{i\delta\omega\Delta\tau} e^{-i\Delta\phi}] + c.c. \\
&= 2|\mathcal{E}|^2 (I_T + I_R)[1 + \mathcal{V} \cos(\delta\omega\Delta\tau - \Delta\phi)],
\end{aligned} \tag{9}$$

where  $\mathcal{V} = \mathcal{V}_0 \mathcal{A}_{TR}(0)$ .

If in any of the two cases above, the self-correlation function can be considered as a constant number. The visibility then only depends on the cross-correlation function and the detector response. If we perform the integration in the frequency domain:

$$\begin{aligned}
\mathcal{V}(\delta\omega) &\approx \mathcal{V}_0 \int d\tau \mathcal{K}(\tau) \mathcal{A}_{TR}(\tau) e^{-i\delta\omega\tau} \\
&= \mathcal{V}_0 \int d\omega \tilde{\mathcal{K}}(\omega) \tilde{\mathcal{A}}_{TR}(\delta\omega - \omega),
\end{aligned} \tag{10}$$

where  $\tilde{\mathcal{K}}(\omega)$ ,  $\tilde{\mathcal{A}}(\omega)$  are the Fourier transforms of  $\mathcal{K}(\tau)$ ,

and  $\mathcal{A}(\tau)$  respectively.  $\tilde{\mathcal{K}}(\omega) = k^2(\omega)$  is the spectral response of the detector, and  $\tilde{\mathcal{A}}(\omega)$  is the pulse spectrum. This is the Eq. (2) of the main text.

*Pulse integration and recovery of the interference pattern.* In the experiment, after every MOT loading, we apply  $N$  measurement pulses. The  $k$ -th pulse starts from the time  $t_1^k$  and ends at  $t_2^k$ . The integrated T and R pulses can be written as  $i_T^k = \int_{t_1^k}^{t_2^k} i_T^k(t) dt$  and  $i_R^k = \int_{t_1^k - \Delta\tau}^{t_2^k - \Delta\tau} i_R^k(t) dt$ , where  $\Delta\tau$  is the storage time. The current addition for the  $k$ -th pulse,  $i_+^k = i_T^k + i_R^k$ , appears when the optical delay is balanced by an electronic delay. Those results are shown in Figs. 2(b)-(g), in which  $i_T$  and  $i_R$  are normalized to keep the splitting ratio as close as possible to 1 : 1. The output power of the HD measurements is commonly recorded by a spectrum analyzer, and is proportional to the average  $\langle i_+^2 \rangle$  over the  $N$  repetitions, i.e.,  $\langle i_+^2 \rangle = (1/N) \sum_k^N (i_+^k)^2$ . From the average of the time-domain power, we get the points in Fig. 2(i), which correspond to the case (I).

For the case (II) of the main text, the direct current addition of T and R pulses after the electronic delay compensation is written as  $i_+^k(t) = i_T^k(t) + i_R^k(t)$ , where  $i_T(t)$  and  $i_R(t)$  have been normalized as above. For the integration of the  $k$ -th pulse from  $t_1^k$  to  $t_2^k$ , we write  $(i_+^k)^2 = \int_{t_1^k}^{t_2^k} [i_+^k(t)]^2 dt$  to get the value of each individual measurement, and compare it with the result of case (I). Finally, the interference pattern is recovered by the average of the total power of the  $N$  repetitions, which is proportional to  $\langle i_+^2 \rangle = (1/N) \sum_k^N (i_+^k)^2$ , as shown in Fig. 3(c).